

The newborn black hole in GRB 191014C proves that it is alive

R. Moradi^{1,2,3}, J. A. Rueda^{1,2,4,5,6}, R. Ruffini^{1,2,7}, and Y. Wang^{1,2,3}

¹ ICRA Net, Piazza della Repubblica 10, 65122 Pescara, Italy

e-mail: rahim.moradi@icranet.org, jorge.rueda@icra.it, ruffini@icra.it

² ICRA, Dipartimento di Fisica, Sapienza Università di Roma, P.le Aldo Moro 5, 00185 Rome, Italy

³ INAF, Osservatorio Astronomico d'Abruzzo, Via M. Maggini snc, 64100 Teramo, Italy

⁴ ICRA Net-Ferrara, Dipartimento di Fisica e Scienze della Terra, Università degli Studi di Ferrara, Via Saragat 1, 44122 Ferrara, Italy

⁵ Dipartimento di Fisica e Scienze della Terra, Università degli Studi di Ferrara, Via Saragat 1, 44122 Ferrara, Italy

⁶ INAF, Istituto de Astrofisica e Planetologia Spaziali, Via Fosso del Cavaliere 100, 00133 Rome, Italy

⁷ INAF, Viale del Parco Mellini 84, 00136 Rome, Italy

Received 18 November 2019 / Accepted 2 April 2021

ABSTRACT

A multi-decade theoretical effort has been devoted to finding an efficient mechanism to use the rotational and electrodynamic energy of a Kerr-Newman black hole (BH), to power the most energetic astrophysical sources such as gamma-ray bursts (GRBs) and active galactic nuclei. We show an efficient general relativistic electrodynamic process which occurs in the “inner engine” of a binary driven hypernova. The inner engine is composed of a rotating Kerr BH of mass M and dimensionless spin parameter α , a magnetic field of strength B_0 aligned and parallel to the rotation axis, and a very low-density ionized plasma. Here, we show that the gravitomagnetic interaction between the BH and the magnetic field induces an electric field that accelerates electrons and protons from the environment to ultrarelativistic energies emitting synchrotron radiation. We show that in GRB 190114C the BH of mass $M = 4.4 M_\odot$, $\alpha = 0.4$, and $B_0 \approx 4 \times 10^{10}$ G can lead to a high-energy (\geq GeV) luminosity of 10^{51} erg s⁻¹. The inner engine parameters are determined by requiring (1) that the BH extractable energy explains the GeV and ultrahigh-energy emission energetics, (2) that the emitted photons are not subjected to magnetic-pair production, and (3) that the synchrotron radiation timescale agrees with the observed high-energy timescale. We find for GRB 190114C a clear jetted emission of GeV energies with a semi-aperture angle of approximately 60° with respect to the BH rotation axis.

Key words. black hole physics – magnetic fields – gamma-ray burst: individual: GRB 190114C – gamma-ray burst: general

1. Introduction

Rotating black holes (BHs) have traditionally been described by the Kerr (Kerr 1963) and the Kerr-Newman metrics (Newman et al. 1965) which assume three conditions: (i) they are in a matter vacuum, (ii) they are embedded in an asymptotically flat spacetime, and (iii) they fulfill global stationarity. Under these conditions, BHs are just a sink of energy, namely “dead BHs”. The discovery of the reversible and irreversible transformations in both these spacetimes (Christodoulou 1970; Christodoulou & Ruffini 1971) opened the conceptual possibility of extracting both rotational and electromagnetic energy from a Kerr-Newman BH. These results also led to the asymptotic mass-energy formula relating the mass M of a BH to three independent parameters, the irreducible mass M_{irr} , the charge Q , and the angular momentum J , soon confirmed by Hawking (1972). The perspective that up to 50% of the mass-energy of a Kerr-Newman BH could be extracted directed the attention to the alternative view of “alive BHs” whose extractable energy could be used as an astrophysical source (see, e.g., “Introducing the black hole” Ruffini & Wheeler 1971a and “On the energetics of black holes” by R. Ruffini in DeWitt & DeWitt 1973).

Since then an efficient process has been sought that is able to power the most energetic astrophysical sources, gamma-ray bursts (GRBs), and active galactic nuclei (AGNs), using the extractable energy from a BH. The theoretical framework has

been constantly evolving (see, e.g., Tursunov & Dadhich 2019, for a review on this topic). As we show in this paper, the recent discovery of the birth of a BH in GRB 130427A (Ruffini et al. 2019a; Rueda & Ruffini 2020) demonstrates that the Kerr BH harbored in the inner engine of this source is indeed an enormous source of giga-electron volt (GeV) energy. The main topic of this article is to reach a deeper understanding of the process of rotational energy extraction by further identifying the astrophysical setting, the boundary conditions, and the basic new physical laws that allow this process to become observable. Specifically, for the case of GRB 190114C, our goal is to infer the values of the independent physical component, the spectral distribution of the high-energy GeV emission, and the geometrical properties of the GeV and ultrahigh-energy emissions.

Our approach is based on the binary-driven hypernova (BdHN) model of long GRBs (Rueda & Ruffini 2012; Fryer et al. 2014; Becerra et al. 2016; Ruffini et al. 2019a). The BdHN progenitor is a binary system composed of a carbon-oxygen (CO) star and a neutron star (NS) companion. The collapse of the iron core of the evolved CO star forms a newborn NS (ν NS) at its center and expels the stellar outermost layers, hence leading to a supernova (SN) explosion. The SN ejecta produces a hypercritical accretion process both onto the ν NS and onto the NS companion. For very compact binaries (orbital period on the order of 5 min), the NS companion reaches the critical mass rapidly (a few seconds), undergoes gravitational collapse,

and forms a rotating BH. We have called these long GRBs in which there is BH formation, BdHNe of type I (BdHN I). Their isotropic energy release is in the range 10^{53} – 10^{54} erg. Numerical simulations of the above process in one, two, and three dimensions have been presented in [Fryer et al. \(2014\)](#), [Becerra et al. \(2015, 2016, 2019\)](#), respectively. Only a fraction of BdHNe form BHs (380 BdHNe I have been identified; see [Ruffini et al. 2021](#)). In progenitors with longer binary periods, on the order of hours, no BHs are formed; the outcome is a binary NS with long GRBs in the range 10^{51} – 10^{53} erg ([Wang et al. 2019](#)). For even longer binary periods, on the order of days, even less energetic long GRBs are encountered, the BdHNe III, for example the case of GRB 060218 ([Liang et al., in prep.](#)).

We now return to GRB 190114C. It has already been shown that the collapse of the CO star, which triggers the complete GRB process in the presence of a binary NS companion, leads to a SN creating an additional NS (i.e., the ν NS). The SN process is observed earlier at X-ray (up to a few keV) and soft gamma-ray (up to a few MeV) wavelengths, and it has been referred to as “SN-rise” (see, e.g., [Wang et al. 2019](#)). For GRB 190114C this occurs in the rest-frame interval $t_{\text{rf}} \lesssim 1.99$ s. It carries an energy of $E_{\text{SN-rise}} = 2.82 \times 10^{52}$ erg and is characterized by a blackbody plus cutoff power-law spectrum ([Liang et al. 2019](#)). The short duration of the SN-rise finds a natural explanation in the BdHN model. In a BdHN I the companion NS is separated at only 10^{10} – 10^{11} cm (i.e., about 1 light-second) from the CO star, implying that only the first spike becomes observable before the expanding SN ejecta triggers the hypercritical accretion process onto the NS companion (see, e.g., [Becerra et al. 2019](#); [Wang et al. 2019](#)).

The newborn BH is embedded in the magnetic field inherited from the NS ([Rueda et al. 2020](#)), and sits at the center of a cavity of very low density (see [Ruffini et al. 2019b](#), for numerical simulations) of material from the SN ejecta. For GRB 190114C such a density has been estimated to be on the order of 10^{-14} g cm $^{-3}$. The cavity is carved during the accretion and subsequent gravitational collapse of the NS leading to the BH. The magnetic field remains anchored to material that did not participate in the BH formation (see [Rueda et al. 2020](#) for a detailed discussion on the magnetic field around the newborn Kerr BH in a BdHN I).

The Kerr BH in the cavity is therefore not isolated and acts in conjunction with a test magnetic field of strength B_0 , aligned with the BH rotation axis. An additional important feature is that there is no vacuum surrounding the BH. As we show in this article, a fully ionized, very low-density plasma is essential to allow the electrodynamic performance of the energy extraction process by the inner engine, which is necessarily non-stationary.

The operation procedure of the inner engine leads the mass and spin of the BH to decrease as functions of time, while the BH irreducible mass (M_{irr}) remains constant. The electrons accelerate to ultrahigh energies at the expense of the BH extractable energy¹

$$E_{\text{extr}} \equiv (M - M_{\text{irr}})c^2, \quad (1)$$

obtainable from the BH mass-energy formula ([Christodoulou 1970](#); [Christodoulou & Ruffini 1971](#); [Hawking 1971](#))

$$M^2 = \frac{c^2}{G^2} \frac{J^2}{4M_{\text{irr}}^2} + M_{\text{irr}}^2, \quad (2)$$

¹ We use cgs-Gaussian units throughout, unless otherwise specified. Careted symbols stand for quantities in geometric units; for example, $\hat{M} \equiv GM/c^2$ denotes geometric mass. See Table 1 for details on the units and conversion factors between the cgs-Gaussian and geometric systems of units.

where J and M are respectively the angular momentum and the mass of the BH.

As we explain in this article, using the mathematical role of the Papapetrou-Wald solution ([Papapetrou 1966](#); [Wald 1974](#)), a profound change of paradigm in relativistic astrophysics has been made possible by the inner engine ([Ruffini et al. 2019a](#)), namely the introduction of the effective charge given by the product of J and B_0 :

$$Q_{\text{eff}} = \frac{G}{c^3} 2JB_0. \quad (3)$$

This effective charge originates from the gravitomagnetic interaction of the Kerr BH with the surrounding magnetic field, left over by the collapse of the accreting NS to the BH still rooted in the surrounding material (see, e.g., [Rueda et al. 2020](#)). The existence of this effective charge finally explains the success of utilizing the concept of a Kerr-Newman BH as a temporary step to approach the analysis of quantum electrodynamic processes in the field of a rotating BH (see, e.g., [Damour & Ruffini 1975](#)).

We are now able to elaborate, with the use of quantum electrodynamics and general relativity, a novel and physically more complete treatment of the GRB high-energy engine in a globally neutral system, therefore satisfying Eq. (2). Starting from these general premises, the main focus of this article is the role of the newborn BH in giving origin to the GeV emission observed by *Fermi*-LAT in the context of the inner engine of a BdHN I. In Sect. 2 we mathematically describe the electromagnetic field surrounding the Kerr BH following the Papapetrou-Wald solution of the Einstein-Maxwell equations ([Papapetrou 1966](#); [Wald 1974](#)). Section 3 summarizes the operation of the inner engine, including its energy budget and electric potential energy available for the acceleration of charged particles around the BH. The particle motion along the BH rotation axis and its relation to the inner engine contribution to ultrahigh-energy cosmic rays (UHE-CRs) is presented in Sect. 4. In Sect. 5 we estimate the energy loss by synchrotron radiation for electrons moving outside the BH rotation axis. We obtain there the typical electron Lorentz factor, the corresponding pitch angles leading to high-energy (\gtrsim GeV) photons, and the radiation timescale. Section 6 presents an estimate of the energy and angular momentum extracted to the Kerr BH in the emission process, in the radiation timescale, implied by the BH mass-energy formula. In Sect. 7 we present our method of inferring the inner engine parameters, namely the BH mass and spin, and the magnetic field strength from the three conditions required (the observed high-energy emission covered by the extractable energy of the BH, the observed high-energy luminosity equal to the synchrotron radiation value, the emitted high-energy photons able to freely escape from the system). In Sect. 8 we apply this framework to the case of GRB 190114C obtaining the corresponding inner engine parameters. Section 9 is dedicated to a comparison of our results with previous literature results. Finally, we outline the conclusions in Sect. 10.

2. Electric and magnetic fields around the BH

Following the considerations presented in [Ruffini et al. \(2015, 2019a\)](#) corresponding to GRB 130427A, we turn to a quantitative estimate of the inner engine via a solution of the Einstein-Maxwell equations of a Kerr BH embedded in a test, asymptotically aligned, uniform magnetic field ([Papapetrou 1966](#); [Wald 1974](#)), hereafter the Papapetrou-Wald solution.

Table 1. Units of the relevant physical quantities used in this article in the cgs-Gaussian and geometric system of units.

	cgs-Gaussian	Geometric	cgs to geometric
M	g	cm	$G/c^2 = 7.425 \times 10^{-29} \text{ cm g}^{-1}$
Q	$\text{cm}^{3/2} \text{ g}^{1/2} \text{ s}^{-1}$ (statC)	cm	$G^{1/2}/c^2 = 2.874 \times 10^{-25} \text{ cm}^{-1/2} \text{ g}^{-1/2} \text{ s}$
J	$\text{g cm}^2 \text{ s}^{-1}$	cm^2	$G/c^3 = 2.477 \times 10^{-39} \text{ g}^{-1} \text{ s}$
Φ	$\text{cm}^2 \text{ g s}^{-2}$ (erg)	cm	$G/c^4 = 8.261 \times 10^{-50} \text{ cm}^{-1} \text{ g}^{-1} \text{ s}^2$
ϕ	$\text{cm}^{1/2} \text{ g}^{1/2} \text{ s}^{-1}$ (statV)	cm^0	$G^{1/2}/c^2 = 2.874 \times 10^{-25} \text{ cm}^{-1/2} \text{ g}^{-1/2} \text{ s}$
E	$\text{cm}^{-1/2} \text{ g}^{1/2} \text{ s}^{-1}$ (statV cm^{-1})	cm^{-1}	$G^{1/2}/c^2 = 2.874 \times 10^{-25} \text{ cm}^{-1/2} \text{ g}^{-1/2} \text{ s}$
B	$\text{cm}^{-1/2} \text{ g}^{1/2} \text{ s}^{-1}$ (gauss, G)	cm^{-1}	$G^{1/2}/c^2 = 2.874 \times 10^{-25} \text{ cm}^{-1/2} \text{ g}^{-1/2} \text{ s}$

Notes. M mass, Q charge, J angular momentum, Φ electric potential energy, ϕ electric potential, E electric field, B magnetic field. We use length (cm) as the base unit in the geometric system.

The BH rotation and the aligned magnetic field induce an electric field with the following radial and polar components:

$$E_{\hat{r}} = \frac{B_0 \hat{a} \hat{M}}{\Sigma^2 A^{1/2}} \left[2r^2 \sin^2 \theta \Sigma - (r^2 + \hat{a}^2)(r^2 - \hat{a}^2 \cos^2 \theta)(1 + \cos^2 \theta) \right], \quad (4a)$$

$$E_{\hat{\theta}} = B_0 \hat{a} \hat{M} \frac{\Delta^{1/2}}{\Sigma^2 A^{1/2}} 2r \hat{a}^2 \sin \theta \cos \theta (1 + \cos^2 \theta). \quad (4b)$$

The magnetic field components are

$$B_{\hat{r}} = \frac{B_0 \cos \theta}{\Sigma^2 A^{1/2}} \left\{ (r^2 + \hat{a}^2) \Sigma^2 - 2\hat{M}r\hat{a}^2 [2r^2 \cos^2 \theta + \hat{a}^2(1 + \cos^4 \theta)] \right\}, \quad (5a)$$

$$B_{\hat{\theta}} = -\frac{\Delta^{1/2}}{\Sigma^2 A^{1/2}} B_0 \sin \theta [\hat{M}\hat{a}^2(r^2 - \hat{a}^2 \cos^2 \theta)(1 + \cos^2 \theta) + r\Sigma^2], \quad (5b)$$

where $\Sigma = r^2 + \hat{a}^2 \cos^2 \theta$, $\Delta = r^2 - 2\hat{M}r + \hat{a}^2$, $A = (r^2 + \hat{a}^2)^2 - \Delta \hat{a}^2 \sin^2 \theta$, and $\hat{M} = GM/c^2$ and $\hat{a} = J/\hat{M} = (GJ/c^3)/(GM/c^2) = J/(Mc)$ are respectively the geometric mass and specific angular momentum of the BH (see Table 1).

We here use the locally non-rotating observer, also known as zero angular momentum observer (ZAMO; see Bardeen 1970; Bardeen et al. 1972). Therefore, the electromagnetic field components ((4a), (4b) and (5a), (5b)) differ from those presented in Ruffini et al. (2019a), where the Carter’s observer was used.

For moderate dimensionless spin values, $\alpha \lesssim 0.7$, where $\alpha \equiv \hat{a}/\hat{M} = cJ/(GM^2)$, the electric and magnetic fields are accurately represented by the first-order expansion ($\alpha \ll 1$ or $\hat{a} \ll \hat{M}$):

$$E_{\hat{r}} \approx -\frac{B_0 \hat{a} \hat{M}}{r^2} (3 \cos^2 \theta - 1), \quad E_{\hat{\theta}} \approx 0, \quad (6a)$$

$$B_{\hat{r}} \approx B_0 \cos \theta, \quad B_{\hat{\theta}} \approx -B_0 \sqrt{1 - \frac{2\hat{M}}{r}} \sin \theta. \quad (6b)$$

Thus, the electric field is mainly radial and inwardly directed. The electric field decreases with the square of the distance; therefore, it is maximum at the BH horizon, $r_+ = \hat{M}(1 + \sqrt{1 - \alpha^2})$, and on the rotation axis $\theta = 0$, so $E_{\hat{r}, \text{max}} = -2B_0 \hat{a}/r_+^2 = -\alpha B_0/2$. The electric field vanishes for $3 \cos^2 \theta_{\pm} - 1 = 0$. Therefore, it is inwardly directed in the northern hemisphere for spherical polar angles (measured clockwise) $-\theta_{\pm} < \theta < \theta_{\pm}$, where $\theta_{\pm} = \arccos(\sqrt{3}/3) \approx 55^\circ$ (see Eqs. (6a), (6b) and Fig. 1). Because of the equatorial symmetry it also points inward in the southern hemisphere for $\pi - \theta_{\pm} < \theta < \pi + \theta_{\pm}$. In these regions, electrons are outwardly accelerated. In the remaining regions the

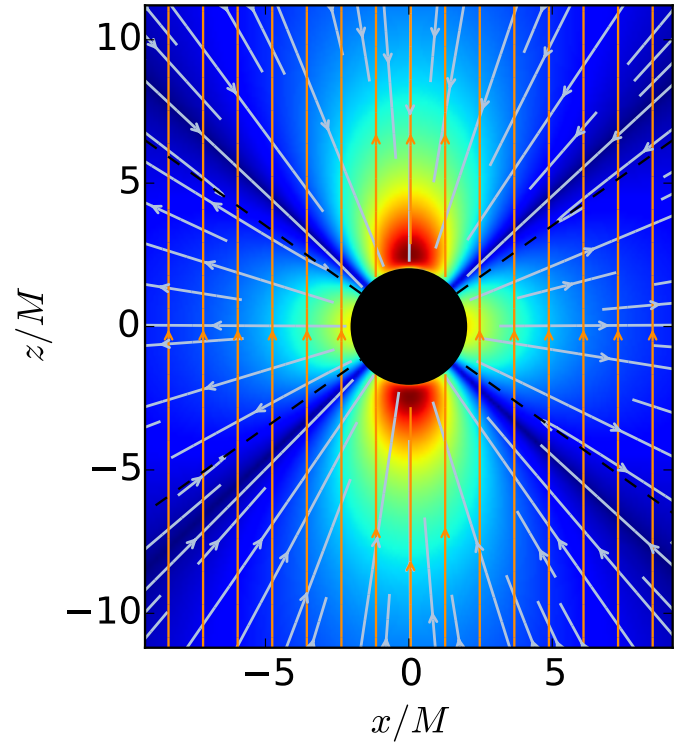


Fig. 1. Electric (blue lines) and magnetic (golden lines) field lines of the Papapetrou-Wald solution in the xz -plane in Cartesian coordinates. The BH spin parameter is set to $a/M = 0.3$ and the magnetic field and the BH spin are aligned and parallel. The background is a density-plot of the electric field energy density which is decreasing from red to blue. The BH horizon is the black disk. Distances are in units of M and the fields in units of B_0 . Outward electron acceleration occurs in the region limited by the dashed black lines, i.e., where the electric field is inwardly directed. In the northern hemisphere it covers spherical polar angles (measured clockwise) $-\theta_{\pm} < \theta < \theta_{\pm}$, where $\theta_{\pm} \approx 55^\circ$. By equatorial symmetry, in the southern hemisphere, it covers $\pi - \theta_{\pm} < \theta < \pi + \theta_{\pm}$.

electric field reverses sign, becoming outwardly directed (see Fig. 1). The value of θ_{\pm} is indeed accurately given by the slow-rotation approximation; for instance, a numerical calculation shows that $\theta_{\pm} \approx 54.74^\circ - 59.76^\circ$ for $\alpha = 0.01 - 0.99$. We show below in this article that, the electrons located in these northern and southern hemisphere cones of semi-aperture angle of $\approx 60^\circ$, are outwardly accelerated with the appropriate pitch angles leading to GeV photons (see Sect. 5 and Fig. 2 for details). Clearly, being anisotropic, this “jetted” emission is not always visible.

This feature has been crucial for the inference of the morphology of the BdHN I from the high-energy (GeV) data of long GRBs (Ruffini et al. 2021).

It can be also seen that the magnetic field is everywhere nearly aligned with the BH rotation axis; at any distance we have $B_z \gg B_x \sim B_y$, and at distances $r \gg 2\hat{M}$ it is perfectly aligned (i.e., $B_x \rightarrow 0$, $B_y \rightarrow 0$, and $B_z \rightarrow B_0$). All these features can be seen in Fig. 1, which shows the electric and magnetic field lines given by the general expressions given by Eqs. (4a), (4b) and (5a), (5b).

3. Operation of the inner engine

The operation of the inner engine is based on three components naturally present in a BdHN I:

- the Kerr metric that describes the gravitational field produced by the newborn rotating BH;
- an asymptotically uniform magnetic field around the newborn BH fulfilling the Papapetrou-Wald solution (see Sect. 2);
- a very low-density plasma around the newborn BH composed of ions and electrons of $10^{-14} \text{ g cm}^{-3}$ (Ruffini et al. 2019b).

The inner engine operation follows these precise steps:

1. The magnetic field and the BH rotation induce an electric field as given by the Papapetrou-Wald solution (see Sect. 2). For an aligned and parallel magnetic field to the BH spin, the electric field is nearly radial and inwardly directed at, and about, the BH rotation axis within an angle θ_{\pm} (see Fig. 1).
2. The induced electric field accelerates electrons outwardly. The number of electrons that can be accelerated is set by the energy stored in the electric field Rueda & Ruffini (2020):

$$\mathcal{E} \approx \frac{1}{2} E_r^2 r_+^3 = \hbar \Omega_{\text{eff}}, \quad (7a)$$

$$\Omega_{\text{eff}} = 4 \left(\frac{m_{\text{Pl}}}{m_n} \right)^8 \left(\frac{B_0^2}{\rho_{\text{Pl}}} \right) \alpha \Omega_+. \quad (7b)$$

Here $\Omega_+ = c^2 \partial M / \partial J = c \alpha / (2 r_+)$ is the so-called BH angular velocity; m_n the neutron mass; and $\rho_{\text{Pl}} \equiv m_{\text{Pl}} c^2 / \lambda_{\text{Pl}}^3$, $\lambda_{\text{Pl}} = \hbar / (m_{\text{Pl}} c)$, and $m_{\text{Pl}} = \sqrt{\hbar c / G}$ are respectively the Planck energy-density, length, and mass. These expressions evidence the nature of the underlying physical process generating the electric field and the BH horizon: the electrodynamics of the Papapetrou-Wald solution (Ruffini et al. 2019a), the origin of its magnetic field from the binary NS companion (Rueda et al. 2020), and the smooth formation of the BH from the induced gravitational collapse process (Rueda & Ruffini 2012). Additional details on the above formulation are presented in Rueda & Ruffini (2020).

3. The maximum possible electron acceleration and energy is set by the electric potential energy difference from the horizon to infinity can be written as (Rueda & Ruffini 2020)

$$\Delta\Phi = \frac{1}{c} e a B_0, = \hbar \omega_{\text{eff}}, \quad (8a)$$

$$\omega_{\text{eff}} = \frac{G}{c^4} 4 \left(\frac{m_{\text{Pl}}}{m_n} \right)^4 e B_0 \Omega_+, \quad (8b)$$

where $a = J/M$.

4. Along the polar axis radiation losses are absent (see below in Sect. 4), while at off-axis latitudes (see below in Sect. 5) the

accelerated electrons emit synchrotron radiation. The radiation timescale τ_{rad} must fulfill

$$\tau_{\text{rad}} = \frac{\mathcal{E}}{L_{\text{GeV}}}, \quad (9)$$

where L_{GeV} is the observed GeV luminosity.

5. After this, the energy \mathcal{E} has been used and emitted. The process restarts with a new angular momentum $J = J_0 - \Delta J$, being ΔJ the angular momentum extracted to the Kerr BH by the event (see below Eqs. (19a)–(19c) in Sect. 6).
6. The above steps are repeated, with the same efficiency, if the density of plasma is sufficient, namely if the number of the particles is enough to cover the new value of the energy \mathcal{E} . Therefore, the inner engine evolves in a sequence of elementary processes, each emitting a well-defined, precise amount of energy.

For the sake of example, let us chose fiducial parameters $B_0 = 10^{11} \text{ G}$, $M = 3 M_{\odot}$, and $\alpha = 0.5$. In this case the available energy is $\mathcal{E} \approx 3.39 \times 10^{37} \text{ erg}$, and the maximum energy that an accelerated electron can gain is $\Delta\Phi \approx 1.06 \times 10^7 \text{ erg} = 6.64 \times 10^{18} \text{ eV}$.

4. Acceleration on the polar axis: Ultrahigh-energy cosmic rays

Along the polar axis, $\theta = 0$, the electric and magnetic fields only have the z -component and are thus parallel; see Eqs. (4a), (4b) and (5a), (5b), or Eqs. (6a) and (6b). Since the electron is accelerated by the electric field, this implies that the electron pitch angle, which is the angle between the electron's injection velocity (into the magnetic field) and the magnetic field, is zero. Consequently, no radiation losses (by synchrotron emission) occur for motion along the BH rotation axis.

The electrons accelerate outward gaining the total electric potential energy, $\Delta\Phi \sim 10^{18} \text{ eV}$. Therefore, the maximum number of electrons that the inner engine can accelerate along the axis is

$$N_{\text{pole}} = \frac{\mathcal{E}}{\Delta\Phi} = \frac{\Omega_{\text{eff}}}{\omega_{\text{eff}}} \sim 10^{31}. \quad (10)$$

These ultrarelativistic electrons contribute to leptonic UHE-CRs. The timescale of this acceleration process along the polar axis is

$$\tau_{\text{pole}} \equiv \frac{\Delta\Phi}{e E_r c} \approx \frac{r_+}{c} = \frac{\alpha}{2\Omega_+} \approx 10^{-5} \text{ s}. \quad (11)$$

This implies that the inner engine can accelerate electrons along the BH rotation axis at a rate

$$\dot{N}_{\text{pole}} \equiv \frac{N_{\text{pole}}}{\tau_{\text{pole}}} \sim 10^{36} \text{ s}^{-1}, \quad (12)$$

leading to a power

$$\dot{\mathcal{E}}_{\text{pole}} = \dot{N}_{\text{pole}} \Delta\Phi = \frac{\mathcal{E}}{\tau_{\text{pole}}} \sim 10^{54} \text{ eV s}^{-1} \approx 10^{42} \text{ erg s}^{-1}. \quad (13)$$

Since the electric and magnetic fields along the rotation axis (and nearly close to it) are parallel (see Fig. 1), the particles in that region are all accelerated (nearly) parallel to the BH rotation axis. Therefore, we do not expect the accelerated particles to have appreciable collisions able to reduce the above estimate of their maximum kinetic energy gain. Therefore, $\dot{\mathcal{E}}_{\text{pole}}$ given by Eq. (13) is the maximum power available for UHECRs.

Table 2. Some astrophysical properties of the inner engine for GRB 190114C and AGN, in the latter adopting as a proxy M 87* (Rueda & Ruffini 2020).

	GRB 190114C	AGN (M 87*-like)
$M (M_{\odot})$	4.4	6.0×10^9
α	0.4	0.1
B_0 (G)	4.0×10^{10}	10
τ_{pole}	4.33×10^{-5} s	0.68 d
$\Delta\Phi$ (eV)	3.12×10^{18}	2.66×10^{17}
\mathcal{E} (erg)	7.02×10^{37}	6.96×10^{44}
$\dot{\mathcal{E}}_{\text{pole}}$ (erg s $^{-1}$)	1.62×10^{42}	1.18×10^{40}
χ ($^{\circ}$)	0.1805–18.05	0.0451–4.51
t_c (s)	1.45×10^{-16} – 1.45×10^{-14}	0.2939–29.39
L_{GeV} (erg s $^{-1}$)	4.83×10^{51} – 4.83×10^{53}	2.37×10^{43} – 2.37×10^{45}

Notes. The timescale of particle acceleration along the BH rotation axis τ_{pole} is given by Eq. (11); the maximum energy gained in such acceleration $\Delta\Phi$ is given by Eqs. (8a) and (8b). The energy \mathcal{E} available for acceleration and radiation is given by Eqs. (7a) and (7b). The maximum power available for acceleration (i.e., to power UHECRs) is $\dot{\mathcal{E}}_{\text{pole}}$ and is given by Eq. (13). The pitch angle χ is computed from Eq. (16) adopting the photon energy range 0.1–1 GeV photons; the corresponding synchrotron radiation timescale t_c is given by Eq. (18), and an estimate of the associated GeV luminosity, $L_{\text{GeV}} \sim \mathcal{E}/t_c$, is also shown. In both cases the corresponding inner engine parameters (BH mass M , spin α , and surrounding magnetic field strength B_0) have been fixed to explain the observed high-energy (\gtrsim GeV) luminosity (see Sect. 7 for the case of GRB 190114C and Rueda & Ruffini 2020 for M 87*).

The extension of the considerations presented here to very massive BHs and AGN, the role of the accretion disk in these galactic configurations, and the possibility of accelerating protons to produce UHECRs by the BH have started to be addressed (Rueda & Ruffini 2020). We compare and contrast in Table 2 some of the inner engine physical properties applied to the case of GRB 190114C and to M 87*.

5. Acceleration at off-axis latitudes: Synchrotron radiation

For the present electric field, and assuming radial motion, the dynamics of the electrons in the electromagnetic field, for $\gamma \gg 1$, is determined from (de Jager et al. 1996; Ruffini et al. 2019a)

$$m_e c^2 \frac{d\gamma}{dt} = e \frac{1}{2} \alpha B_0 c - \frac{2}{3} e^4 \frac{B_0^2 \sin^2 \langle \chi \rangle}{m_e^2 c^3} \gamma^2, \quad (14)$$

where e is the elementary charge, γ is the electron Lorentz factor, $\langle \chi \rangle$ is the injection angle between the direction of electron motion and the magnetic field (the pitch angle), and m_e is the electron mass. This equation is integrated assuming the electrons are injected near the horizon (where the electric field strength is $\alpha B_0/2$), for selected values of the injection angle $\langle \chi \rangle$, with an initial Lorentz factor $\gamma = 1$ at $t = 0$.

The synchrotron spectrum peaks roughly at the photon critical energy (see, e.g., Landau & Lifshitz 1975)

$$\epsilon_{\gamma} = \frac{3e\hbar}{2m_e c} B_0 \sin \langle \chi \rangle \gamma^2 = \frac{3}{2} m_e c^2 \beta \sin \langle \chi \rangle \gamma^2, \quad (15)$$

where in the last expression we introduced $\beta = B_0/B_c$, with $B_c = m_e^2 c^2 / (e\hbar) \approx 4.41 \times 10^{13}$ G. Therefore, the synchrotron peak energy shifts from lower to higher energies (soft-to-hard spectral evolution) as the electron accelerates. For example, the photon critical energy ϵ_{γ} , for $\gamma \gtrsim 10^3$, a magnetic field $B_0 = 10^{11}$ G (so $\beta = 0.0023$), and a pitch angle $\chi = 10^{\circ}$ falls in the GeV regime.

During the acceleration, the Lorentz factor increases linearly with time up to an asymptotic maximum value (see Ruffini et al.

2019a, for details). This maximum value, set by the balance between the energy gain by acceleration in the electric field and energy loss by synchrotron radiation, is (Ruffini et al. 2019a)

$$\gamma_{\text{max}} = \frac{1}{2} \left[\frac{3}{e^2 / (\hbar c)} \frac{\alpha}{\beta \sin^2 \langle \chi \rangle} \right]^{1/2}, \quad (16)$$

which defines the maximum electron energy $\epsilon_e = \gamma_{\text{max}} m_e c^2$. Associated with γ_{max} , by replacing Eq. (16) into (15) we obtain the maximum peak energy of the spectrum (Ruffini et al. 2019a)

$$\epsilon_{\gamma, \text{max}} = \frac{9}{8} \frac{m_e c^2}{e^2 / \hbar c} \frac{\alpha}{\sin \langle \chi \rangle} \approx \frac{78.76}{\sin \langle \chi \rangle} \alpha \text{ MeV}, \quad (17)$$

and the synchrotron cooling timescale $t = t_c$ for the above maximum photon critical energy is given by (Ruffini et al. 2019a)

$$t_c = \frac{\hbar}{m_e c^2} \frac{3}{\sin \langle \chi \rangle} \left(\frac{e^2}{\hbar c} \alpha \beta^3 \right)^{-1/2}. \quad (18)$$

For model parameters $\alpha = 0.5$ and $B_0 = 10^{11}$ G, photons of energy 0.1–10 GeV (typical photon energy range detected by the *Fermi*-LAT) are emitted by electrons with pitch angles $\chi \approx 0.23$ – 23° , and electron energy $\epsilon_e = 1.98 \times 10^8$ – 1.98×10^{10} eV, radiating on a timescale of $t_c = 2.63 \times 10^{-17}$ – 2.63×10^{-15} s. We show in Fig. 2 the pitch angle χ as a function of the maximum photon critical energy (spectrum peak energy) $\epsilon_{\gamma, \text{max}}$, obtained from Eq. (17), in the energy range 0.1–10 GeV, and for three selected values of α . Figure 3 shows the contours of constant χ for electrons moving in the electromagnetic field of the Papapetrou-Wald solution shown in Fig. 1. In particular, we show pitch angles for which electrons emit photons of GeV energies (see also Fig. 2). It can be seen that this high-energy jetted emission occurs within an effective opening angle $\theta_{\pm} \approx 60^{\circ}$. This anisotropic emission is essential to infer the BdHN I morphology from the GeV emission data of long GRBs (Ruffini et al. 2021).

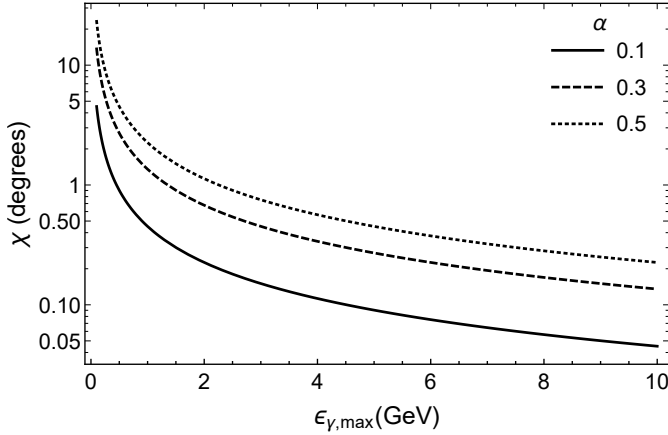


Fig. 2. Pitch angle χ (in units of degrees) as a function of the photon critical energy ϵ_γ (in units of GeV) obtained from Eq. (17). The focus of the plot for photon critical energy is in the range 0.1–10 GeV. The solid, dashed, and dotted curves correspond to selected values of the BH spin parameter $\alpha = 0.1, 0.3,$ and $0.5,$ respectively.

6. Energy and angular momentum extraction, golden rule, and duration of the inner engine activity

At the end of every elementary process, all the energy \mathcal{E} has been emitted. The inner engine restarts its operation with the same magnetic field of B_0 , but with a new slightly smaller angular momentum $J = J_0 - \Delta J$, being ΔJ the angular momentum extracted by the process. From the BH mass-formula (2), keeping the irreducible mass constant (i.e., $\Delta M_{\text{irr}} = 0$, and $\Delta Mc^2 = \mathcal{E}$), we obtain a change in the BH angular momentum ΔJ in each event:

$$J_{\text{eff}} = I_{\text{eff}} \Omega_{\text{eff}}, \quad I_{\text{eff}} = M \left(\frac{2GM_{\text{irr}}}{c^2} \right)^2, \quad (19a)$$

$$\Delta J = \frac{J_{\text{eff}}}{J} \hbar, \quad (19b)$$

$$\Delta J = \frac{1}{\Omega} \Delta E, \quad \bar{\Omega} \equiv \frac{J}{I_{\text{eff}}}, \quad \Delta E \equiv \mathcal{E}. \quad (19c)$$

Here the last equation, a truly golden formula, relates the energy radiated ($\Delta E = \mathcal{E}$) to the angular momentum extracted to the rotating BH (ΔJ).

For the fiducial parameters that we used above, $M = 3 M_\odot$, $\alpha = 0.5$, and $B_0 = 10^{11}$ G, we have $J \approx 3.96 \times 10^{49}$ g cm² s⁻¹, $M_{\text{irr}} \approx 2.9 M_\odot$, and $\Delta J \approx 1.0 \times 10^{33}$ g cm² s⁻¹, so a fractional change $\Delta J/J \approx 10^{-16}$, implying that the activity can last for thousands of years or more, providing there is ionized plasma to feed the inner engine.

7. Inference of the BH mass, spin, and surrounding magnetic field

We require three physical and astrophysical conditions to obtain the three inner engine parameters, the BH mass and spin, M and α , and the strength of the magnetic field surrounding the BH, B_0 . Following Ruffini et al. (2019a), who show that the use of solely the GeV emission data, after the ultrarelativistic prompt emission (UPE) phase (see Liang et al. 2019), is enough to determine the inner engine parameters (see Fig. 4). In particular, we show that this procedure serves to obtain a lower limit to the mass

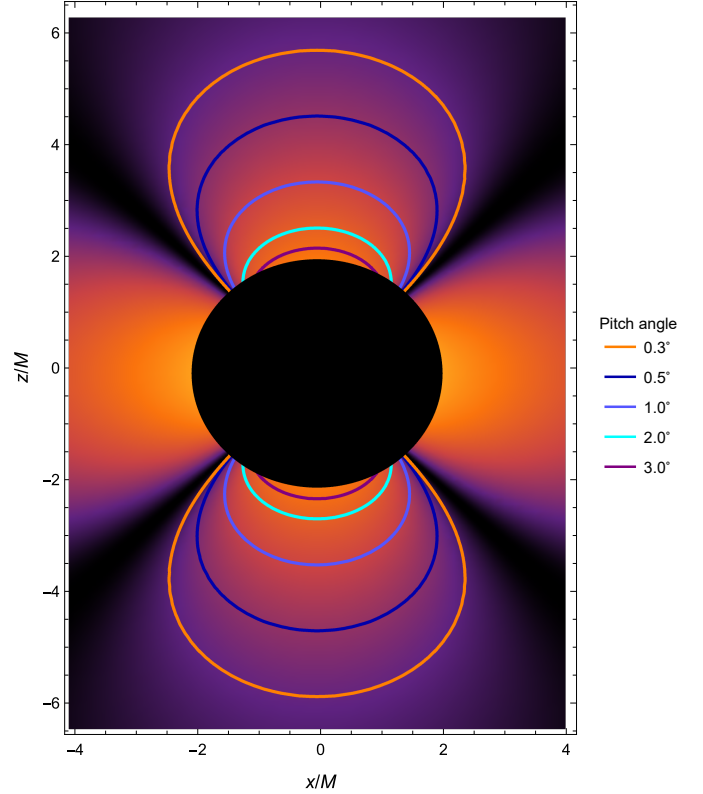


Fig. 3. Contours of constant pitch angle (χ) of electrons moving in the electromagnetic field of the Papapetrou-Wald solution shown in Fig. 1. For the present magnetic dominated case ($|E|/|B| < 1$), charged particles follow the magnetic field lines; therefore, $\sin \chi = |\mathbf{B}|^{-1} \sqrt{(\mathbf{E} + \mathbf{v} \times \mathbf{B}/c)^2 - (\mathbf{v} \cdot \mathbf{E})^2/c^2} \approx \sqrt{|\mathbf{E}|^2/|\mathbf{B}|^2 - |\mathbf{E}_\parallel|^2/|\mathbf{B}|^2} \approx |\mathbf{E}|/|\mathbf{B}| \sin \Psi$ (see, e.g., Kelner et al. 2015), where \mathbf{E}_\parallel is the electric field component parallel to the magnetic field, and Ψ is the angle between \mathbf{B} and $-\mathbf{E}$ (the minus sign is used because we are interested in the pitch angle of electrons). In the slow-rotation regime (see Eqs. (6a) and (6b)), $\sin \Psi \approx \sin \theta/(1 - 2M \sin^2 \theta/r)$, so $\sin \chi \approx |\mathbf{E}|/|\mathbf{B}| \sin \theta/(1 - 2M \sin^2 \theta/r)$. The BH is indicated by the black disk. The background color map indicates the electric field energy density (lighter colors means more intense).

and spin of the BH. The most important point is that we obtain the value of the irreducible mass of the BH that is kept constant through the energy extraction process. This allows us to determine the time evolution of the BH mass and spin. This can be achieved by fulfilling the three following conditions.

7.1. Condition 1

First, we require that the rotational energy of the BH provides the energy budget for the observed GeV emission energetics,

$$E_{\text{extr}} \geq E_{\text{GeV}}, \quad (20)$$

which via Eqs. (1) and (2) leads to the following inequality between M , α , and E_{GeV} :

$$M \geq \frac{1}{\eta} \frac{E_{\text{GeV}}}{c^2}, \quad \eta \equiv 1 - \sqrt{\frac{1 + \sqrt{1 - \alpha^2}}{2}}. \quad (21)$$

We recall that the maximum value of the efficiency parameter is $\eta_{\text{max}} \approx 0.293$, which is attained for a maximally rotating BH, $\alpha_{\text{max}} = 1$. It is also important to recall that, by keeping the BH irreducible mass constant in the energy extraction process, we

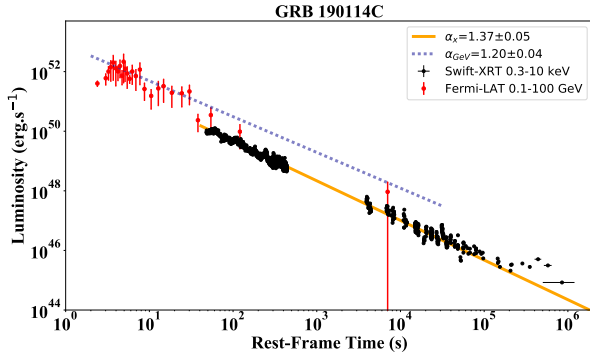


Fig. 4. Red data points: rest-frame 0.1–100 GeV luminosity light curve of GRB 190114C during and after UPE phase obtained from *Fermi*-LAT. Green dashed line: best fit for power-law behavior of the luminosity following the UPE phase with slope of 1.2 ± 0.04 and amplitude of $7.75 \pm 0.44 \times 10^{52}$ erg s $^{-1}$. Black data points: rest-frame 0.3–10 keV luminosity expressed in the rest frame obtained from *Swift*-XRT. It follows a power-law behavior with an amplitude of $A_X = (5.14 \pm 2.03) \times 10^{52}$ erg s $^{-1}$ and a slope of $\alpha_X = 1.37 \pm 0.05$.

are inferring a lower limit to the BH mass. An increasing M_{irr} with time implies a higher BH mass to explain the same GeV energetics.

7.2. Condition 2

We require that the GeV photons must be transparent to the magnetic e^+e^- pair creation process. The attenuation coefficient for this process is (see [Daugherty & Harding 1983](#) and Sect. 5 in [Ruffini et al. 2019a](#))

$$\bar{R} \sim 0.23 \frac{e^2}{\hbar c} \left(\frac{\hbar}{m_e c} \right)^{-1} \beta \sin \langle \chi \rangle \exp \left(-\frac{4}{3} \psi \right), \quad (22)$$

where $\psi = \beta \sin \langle \chi \rangle \epsilon_\gamma / (2m_e c^2)$. Substituting Eq. (17) into Eq. (22), \bar{R} becomes a function of ϵ_γ and the product $\alpha\beta$. For a given ϵ_γ and α , the lower the magnetic field, the larger the mean free path \bar{R}^{-1} , as expected. When $\chi \ll 1$, the exponential term dominates, hence \bar{R}^{-1} exponentially increases tending to become infinite. An order-of-magnitude estimate of the magnetic field can be obtained by requiring $\psi \ll 1$,

$$\beta \ll \frac{16 e^2}{9 \hbar c \alpha} \frac{1}{\alpha} \approx \frac{1.298 \times 10^{-2}}{\alpha}, \quad \text{or} \quad B_0 \ll \frac{5.728 \times 10^{11}}{\alpha} \text{ G}, \quad (23)$$

which is independent of the photon peak energy. It should be noted that this constraint already restricts the magnetic field to be undercritical ($\beta < 1$), and as we shall see it is sufficient for explaining the GeV emission after the UPE phase. The constraint (23) is analogous to imposing a lower limit on \bar{R}^{-1} . For instance, adopting a photon energy of 0.1 GeV, it can be checked that for $\alpha\beta = 1.298 \times 10^{-2}$, the mean free path is $\bar{R}^{-1} = 1.17 \times 10^5$ cm. Lower values of $\alpha\beta$ lead to much larger values of \bar{R}^{-1} . It is very interesting that this value is comparable to $GM_\odot/c^2 \approx 1.477 \times 10^5$ cm. Therefore, requesting a value of $\alpha\beta$ lower than the above-mentioned one, implies having a mean free path that is much larger than the BH horizon. Specifically, the high-energy photons are produced in the vicinity of the BH, but they can freely escape from the system. If we adopt as a fiducial value that 0.1 GeV photons have a sufficiently large mean free

path (e.g., $\bar{R}^{-1} \geq 10^{16}$ cm), we obtain ([Ruffini et al. 2019a](#))

$$\beta \leq \frac{3.737 \times 10^{-4}}{\alpha}, \quad \text{or} \quad B_0 \leq \frac{1.649 \times 10^{10}}{\alpha} \text{ G}. \quad (24)$$

That we are in the exponentially increasing part of the mean free path is evident by the fact that, by requesting a mean free path which is 11 orders of magnitude larger than the one implied by (23), our upper limit to the magnetic field is decreased less than one order of magnitude. Therefore, our estimate of the magnetic field is not sensitive to the choice of the value of \bar{R}^{-1} , providing it satisfies $\geq 10^5$ cm. This implies that the magnetic field strength of the inner engine is constrained to have a value, roughly speaking, in the range 10^{10} – 10^{11} G (see Fig. 5).

7.3. Condition 3

The third condition (i.e., the closure equation) is obtained by requesting that the timescale of the synchrotron radiation, the cooling time t_c given by Eq. (18), be equal to the observed GeV emission timescale ([Ruffini et al. 2019a](#))

$$\tau_{\text{rad},1} = \frac{\mathcal{E}_1}{L_{\text{GeV},1}}, \quad (25)$$

where \mathcal{E} is the electrostatic energy available for the process (see Eqs. (7a) and (7b)). The subscript “1” refers to quantities evaluated at the beginning of the transparency of the GeV emission (i.e., at the end of the UPE phase) at $t = t_{\text{tr, UPE}}$ (see Sect. 8). We refer to this as the first elementary impulsive event. Therefore, the third equation of the system is

$$t_c(\langle \chi \rangle, \alpha, \beta) = \tau_{\text{rad},1}(\mu, \alpha, \beta, L_{\text{GeV},1}), \quad (26)$$

where $\mu = M/M_\odot$ and M_\odot is the solar mass.

Therefore, having imposed these three conditions, we obtain the three inner engine parameters from the system of Eqs. (21), (24), and (26), as follows:

1. We adopt the equality in Eq. (21), which implies that we will obtain a lower limit to the BH and spin;
2. We replace it into the equality of Eq. (24), which implies that we are adopting the upper limit to the magnetic field strength (for a given α);
3. We obtain the following expression for β as a function of α and of the observables E_{GeV} and L_{GeV} ([Ruffini et al. 2019a](#)):

$$\begin{aligned} \beta &= \beta(\epsilon_\gamma, E_{\text{GeV}}, L_{\text{GeV},1}, \alpha) \\ &= \frac{1}{\alpha} \left(\frac{64}{9} \sqrt{3} \frac{e^2}{\hbar c} \frac{\epsilon_\gamma}{B_c^2 r_+(\mu, \alpha)^3} \frac{L_{\text{GeV},1}}{e B_c c^2} \right)^{2/7}, \end{aligned} \quad (27)$$

where we have substituted Eq. (17) into Eq. (18) to express t_c as a function of the peak photon energy ϵ_γ , instead of the pitch angle χ .

Therefore, the BH horizon r_+ is a function of μ and α , but in view of Eq. (21) it becomes a function of E_{GeV} and α . Given the observational quantities E_{GeV} (integrated after the UPE phase) and the luminosity $L_{\text{GeV},1}$ (at the end of the UPE phase), Eq. (27) gives a family of solutions of β as a function of α . The solution of this equation together with Eq. (24) gives the values of β and α . With the knowledge of α and E_{GeV} , we obtain μ from Eq. (21).

8. Application to GRB 190114C

We now turn to apply the above procedure to GRB 190114C. For the observational properties of this source we follow the

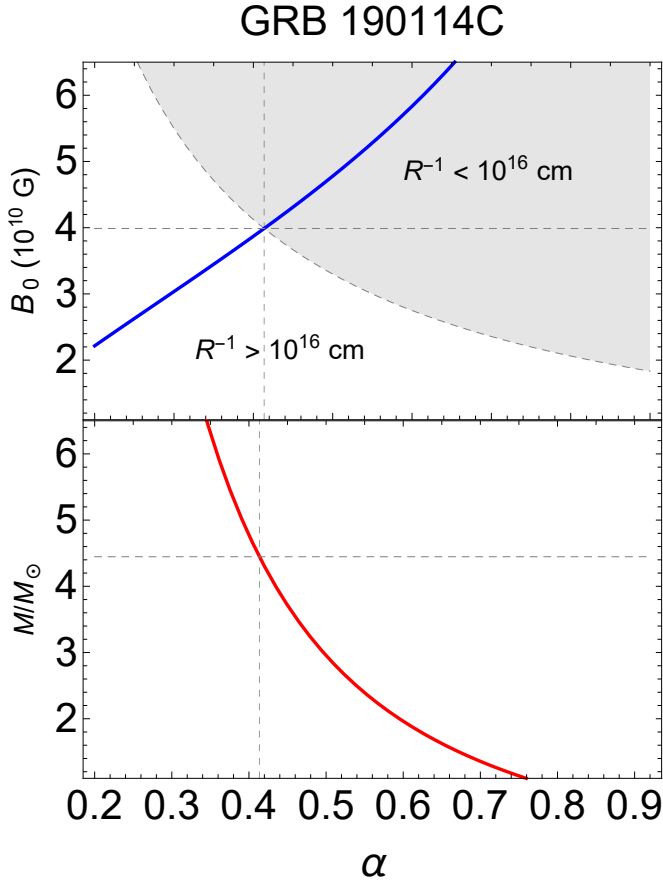


Fig. 5. Parameters of the inner engine of GRB 190114C. For this source we have $L_{\text{GeV},1} = 1.47 \times 10^{52} \text{ erg s}^{-1}$ and $E_{\text{GeV}} = 1.8 \times 10^{53} \text{ erg}$. *Upper panel:* family of solutions of B_0 as a function of α (blue curve), given by Eq. (27). We use here a photon energy $\epsilon_\gamma = 0.1 \text{ GeV}$ (lower edge of the *Fermi*-LAT energy band). In the gray shaded region the mean free path is $\bar{R}^{-1} < 10^{16} \text{ cm}$, while in the white shaded region it is $\bar{R}^{-1} \geq 10^{16} \text{ cm}$. The curve separating the two regions is therefore given by the equality in (24). *Lower panel:* corresponding family of solutions $M(\alpha)$ (red curve), given by Eq. (21).

results of Liang et al. (2019). The UPE phase has been shown in that paper to end at the rest-frame time $t_{\text{rf, UPE}} = 3.99 \text{ s}$, so we limit our analysis to longer times. Therefore, for GRB 190114C, we have $t_{\text{rad},1} = t_{\text{rf, UPE}} = 3.99 \text{ s}$. The 0.1–100 GeV luminosity observed by *Fermi*-LAT, at $t \geq t_{\text{rf, UPE}}$, is well fitted by a power-law function analogous to the case of GRB 130427A (Ruffini et al. 2019a) (see our Fig. 4):

$$L_{\text{GeV}} = A t^{-n} = (7.75 \pm 0.44) \times 10^{52} t^{-(1.2 \pm 0.04)} \text{ erg s}^{-1}. \quad (28)$$

The associated integrated isotropic energy observed by *Fermi*-LAT, from $t_1 = t_{\text{rf, UPE}} = 3.99 \text{ s}$ to $\sim 10^4 \text{ s}$, is $E_{\text{GeV}} = (1.8 \pm 1.3) \times 10^{53} \text{ erg}$, and the luminosity at $t = t_{\text{rad},1}$ is $L_{\text{GeV},1} = 1.47 \times 10^{52} \text{ erg s}^{-1}$ (see Liang et al. 2019).

For the above numbers, and assuming the minimum energy budget requirement, specifically assuming the equality in Eq. (20), the inner engine parameters are (see Fig. 5) magnetic field $B_0 \approx 3.9 \times 10^{10} \text{ G}$, and spin and BH mass $\alpha = 0.41$ and $M = 4.45 M_\odot$, respectively. The corresponding BH irreducible mass is $M_{\text{irr}} = 4.35 M_\odot$. For the above spin value, Eq. (17) leads to a pitch angle for the emission of 0.1 GeV photons, $\theta \approx \pi/9$.

The inequality (20) implies that the above mass and spin values of the BH must be considered as lower limits. As we show in Sect. 6, the inner engine can be long-lasting so it can continue

to emit and so will eventually radiate more than the observed E_{GeV} that we have used limiting ourselves to the first 10^4 s of emission. However, in view of the power-law behavior of the GeV luminosity, most of the energy is emitted in this early evolution so the BH parameters do not change significantly if we consider the extrapolation of the energy budget. For example, let us assume that the power-law luminosity (28) extends for 1000 yr. This would increase the total GeV energy radiated by 25%, and recalculating all the parameters we obtain $\alpha = 0.46$, $M = 4.50 M_\odot$, and $M_{\text{irr}} = 4.38 M_\odot$.

9. Comparison with previous literature

9.1. Long GRBs in the traditional model

We first recall some key features of the traditional model of long GRBs. To this end, we are facilitated by the book by Bing Zhang (Zhang 2018), which includes an extensive number of references. The traditional GRB model roots can be found in the papers by Rees & Meszaros (1992), Mészáros & Rees (1997), and Woosley (1993). The model proposed by Rees & Meszaros (1992) is based on a single system: GRBs are explained by a single BH from which an ultrarelativistic blastwave originates and whose expansion follows the Blandford–McKee self-similar solution (Blandford & McKee 1976). Woosley (1993) connected the GRB origin to a Kerr BH emitting an ultrarelativistic jet that originates from matter accretion onto the BH. The BH was proposed to form from the direct collapse of a massive star, called a failed SN or a “collapsar”, leading to a BH in the mass range $5\text{--}10 M_\odot$.

In these models the afterglows are explained via the kinetic energy of the ultrarelativistic blastwave, which can reach very high bulk Lorentz factors, $\Gamma \sim 1000$, to be released when it interacts with the circumburst medium (Waxman & Piran 1994; Sari & Piran 1995; Wijers et al. 1997; Sari 1997; Sari et al. 1998). The observed spectrum is proposed to be produced by synchrotron and synchrotron self-Compton (SSC) emission from accelerated electrons during the deceleration of the ultrarelativistic blastwave radiating at distances $10^{16}\text{--}10^{18} \text{ cm}$. As pointed out by Zhang (2018), these models based on an ultrarelativistic blastwave radiating at distances $10^{16}\text{--}10^{18} \text{ cm}$ have been applied to jointly explain in the jetted emission several observations:

1. the X-ray afterglow, the steep and shallow decay of the luminosity in the Nousek-Zhang phase (Nousek et al. 2006; Zhang et al. 2006), the X-ray flares and the gamma-ray flares;
2. the emission in the MeV and in the keV observed by the *Neils Gehrels Swift* Observatory, as well as the emission in the optical and in the radio, as well as the emission in the TeV recently observed by MAGIC (Mirzoyan et al. 2019; MAGIC Collaboration 2019a,b);
3. the high-energy (GeV) emission observed in some long GRBs by *Fermi*-LAT.

Within the traditional model, all the above emissions are explained using solely the kinetic energy of the ultrarelativistic blastwave with $\Gamma \sim 10^3$, and radiating at $10^{16}\text{--}10^{18} \text{ cm}$. It becomes clear that, requiring to the single kinetic energy of an ultrarelativistic blastwave to account for the entire energetics of all the observed radiation, at all wavelengths, from the prompt to the afterglow, results in an extreme request to the energy reservoir of the GRB engine.

Within the traditional collapsar-fireball model, the presence of a mildly relativistic expanding component has been introduced in Ramirez-Ruiz et al. (2002), called a cocoon, which

moves sideways to the jet. However, as is clearly elucidated in [Nakar & Piran \(2017\)](#); see also references therein), the emission in the X-rays from this cocoon is too low with respect to be observed X-ray afterglow of long GRBs, unless the cocoon Lorentz factor becomes $\Gamma > 10$. The possibility of a mildly relativistic component in the traditional model is interesting for its implications for the nature of the low-energy sources such as GRB 060218 (see, e.g., [Nakar 2015](#)). These sources have energies $10^{49} - 10^{51}$ erg, which is the range of energies of BdHNe II and III. However, this is beyond the scope of this article, which is dedicated to BdHNe I, which are characterized by the energy range $10^{52} - 10^{54}$ erg. In conclusion, an explanation of the X-ray afterglow in the traditional model needs ultrarelativistic values of the Lorentz factor (see also [Zhang 2018](#), for a review on the subject).

9.2. Long GRBs in the BdHN model

As we note in Sect. 1, the BdHNe have a binary progenitor composed of a CO star and a companion NS. The GRB is composed of independent physical process identified by a time-resolved spectral analysis. Some key results are the following:

1. In the analysis of the data of the XRT detector on board the *Neils Gehrels Swift* satellite of the gamma-ray flare, the X-ray flares, the flare-plateau, and the early afterglow phases (the Nousek-Zhang phase), after the ultrarelativistic prompt radiation phase, showed that the emitter in these phases is in mildly relativistic expansion with $\Gamma \lesssim 5$ (see [Ruffini et al. 2018a](#), for details). A similar upper limit $\Gamma \lesssim 3$ was obtained in the case of GRB 151027A ([Ruffini et al. 2018b](#)), and for GRB 130427A the corresponding upper limit on the bulk Lorentz factor is $\Gamma \lesssim 2$ ([Ruffini et al. 2018c](#)). Therefore, these stringent upper limits on Γ exclude any ultrarelativistic motion following the UPE phase, contrary to the prediction of traditional GRB models based on the ultrarelativistic blastwave.
2. The high-energy GeV emission follows from the action of the inner engine presented in this work, powered by the BH rotational energy extraction process. In the case of GRB 190114C studied in this work, this corresponds to $t_{\text{rf}} \gtrsim 3.99$ s (see Fig. 4 and [Liang et al. 2019](#)). It is characterized by an afterglow in the GeV radiation which, when expressed in the rest frame, follows a power-law luminosity (see Eq. (28) and Fig. 4), and it carries an energy of $E_{\text{GeV}} = (1.8 \pm 1.3) \times 10^{53}$ erg.
3. In parallel, the X-ray afterglow emission observed by the *Swift* satellite originates from the synchrotron radiation produced in the expanding SN ejecta, threaded by the magnetic field of the ν NS, and aided by the injection of particles and the pulsar-like radiation from the ν NS into the SN ejecta ([Ruffini et al. 2018c](#); [Wang et al. 2019](#); [Rueda et al. 2020](#)). These processes are mainly powered by the rotational energy of the ν NS and have led to a significant progress in understanding the origin of the X-ray afterglow emission (see, e.g., the case of GRB 130427A in [Ruffini et al. 2018c](#), and GRB 160509A, GRB 160625B, GRB 180728A, and GRB 190114C in [Rueda et al. 2020](#)). In these analyses the spin of the ν NS and the strength and structure of its magnetic field have been inferred. In the case of GRB 190114C, the luminosity expressed in the rest frame follows a power-law behavior $L_X = A_X t^{-\alpha_X}$, where $A_X = (5.14 \pm 2.03) \times 10^{52}$ erg s $^{-1}$ and $\alpha_X = 1.37 \pm 0.05$ and carries an energy $E_X = 2.11 \times 10^{52}$ erg; see Fig. 4 ([Ruffini et al. 2021](#); see also [Liang et al. 2019](#)). This interpretation of the X-ray afterglow

in the BdHN model conforms with the observational upper limits on the Γ factor of the X-ray afterglow emitter summarized in point 1 above (see [Ruffini et al. 2018a](#), for details).

In this way, being the total energetics divided into the different components of the system and their associated different physical phenomena, the energetic request to each emission episode in the BdHN becomes affordable.

9.3. Process of BH energy extraction

Having indicated the main differences between the traditional GRB model and the BdHN model regarding the X-ray and the GeV afterglow emissions, we focus now on the mechanism of the high-energy (GeV) emission, which is intimately related to the physics of the GRB central engine.

There is a vast literature devoted to magnetic fields around BHs and how they may act in a mechanism that could extract the rotational energy of a Kerr BH. An early attempt in the absence of a charge by a matter-dominated magnetized plasma accreting in a disk around a pre-existing Kerr BH was presented in [Ruffini & Wilson \(1975\)](#). The effective potential describing the circular orbit of massive particles around a Kerr BH was adopted (see [Ruffini & Wheeler 1971b](#), in problem 2 of Sect. 104 in [Landau & Lifshitz 1975](#)). The infinite conductivity condition, $F_{\mu\nu}u^\nu = 0$, where $F_{\mu\nu}$ is the electromagnetic field tensor and u^ν the plasma four-velocity, was used there leading to $E \cdot B = 0$. Under these conditions, the acceleration of particles and processes of energy extraction were not possible.

This work was further developed by [Blandford & Znajek \(1977\)](#); in order to overcome the condition $E \cdot B = 0$ in the magnetosphere, they adopted the concepts of gaps and spontaneous e^+e^- pair creation, closely following the seminal ideas of pulsar theory by [Sturrock \(1971\)](#) and [Ruderman & Sutherland \(1975\)](#). They imposed a force-free condition, $F_{\mu\nu}J^\nu = 0$, where J^ν is the current density, as well as gaps outside the BH horizon. The aim was to produce an ultrarelativistic matter-dominated plasma whose bulk kinetic energy could be used to explain the energetics of a jet at large distances from the BH.

There is also another direction in the literature following the work of [MacDonald & Thorne \(1982\)](#). It extends the work of [Blandford & Znajek \(1977\)](#) and looks at the problem of matter-dominated accretion in presence of a magnetic field anchored to a rotating surrounding disk. Specifically, they proposed an analogy of a rotating BH immersed in a magnetic field with a rotating conductive sphere and/or with the analogy of such a BH and the surrounding magnetosphere as an electric circuit. Independent of the analogies, the underlying physical system remains the same as that proposed by [Blandford & Znajek \(1977\)](#).

The present model is mainly motivated by fitting the GeV emission of GRBs. There is no matter-dominated disk accretion. There is instead a very low-density ionized plasma fulfilling an acceleration electro-dynamical process around a newly born BH. We use the Papapetrou-Wald solution in which the electromagnetic field is naturally characterized by regions where $E \cdot B \neq 0$ (see Sect. 2, Fig. 1, and [Wald 1974](#)). This feature naturally allows the acceleration of particles without the need of introducing any gaps. There is no ultrarelativistic matter-dominated plasma outflow. The accelerated charged particles emit synchrotron-radiation photons that carry off energy and angular momentum close to the BH. The BH in our scenario is not pre-existing: it is smoothly formed by the hypercritical accretion onto the binary companion NS. The magnetic field, characterizing the Papapetrou-Wald solution, is amplified during the process of gravitational collapse of the binary companion NS

(Rueda et al. 2020). There is no room in this model for the gravitational stable circular orbits around the Kerr BH. The particles are accelerated by an ultrarelativistic electro-dynamical process.

Our description is also different with respect to recent GRB literature. For instance, in Metzger et al. (2011), Beniamini et al. (2017), and references therein, the presence of a magnetized wind, outflow, or jet is powered by a central engine. In these works the engine is represented by a NS endowed with an ultra-high magnetic field, a magnetar, that loses its rotational energy via magnetic-dipole braking, in complete analogy to pulsars. The magnetar powers the outflows that produce the GRB emission at large radii on the order of 10^{15} cm. These models focus on the explanation of the (MeV) GRB prompt and the (X-ray) afterglow emission using the rotational energy of a magnetar, so they do not look either to the physics of BHs, or to the GeV emission that are the topics of the present article.

The understanding of the complex nature of a BdHN requires the knowledge of different episodes, which in some cases are strictly independent, and their description can occur independently of each other.

For instance, the existence of hyper-energetic SN, the SN-rise, radiates off 10^{52} erg in the case of GRB 190114C (Liang et al. 2019). In parallel, the interaction of the SN ejecta with the magnetic field of the ν NS and its pulsar-like emission, explain the observed X-ray afterglow (Ruffini et al. 2018c; Wang et al. 2019; Rueda et al. 2020). This emission is produced at distances 10^{12} – 10^{16} cm from the binary progenitor.

In the present work we address the most energetic GRB component, the GeV emission originating close to the horizon, at distances of 10^6 cm, starting in the case of GRB 190114C at a rest-frame time of 3.99 s after the trigger.

After the clarification of these concepts, we will be ready to describe the optically thick sub-MeV emission in the time interval 1.99–3.99 s, which comprises the 55% of the energy of GRB 190114C, overcoming the compactness problem using our classic approach of the fireshell model (see Ruffini et al. 1999, 2000; Bianco et al. 2001; Moradi et al., in prep.).

10. Conclusions

The inner engine theory applied in this work to GRB 190114C represents an authentic full paradigm shift from the traditional model of long GRBs based on the emission of an ultrarelativistic blastwave, somehow powered by a Kerr BH. It seems too expensive for nature to accelerate matter in bulk, against the gravitational pull of the BH, to a large distance of $\sim 10^{16}$ – 10^{17} cm and with $\Gamma \sim 10^3$ to guarantee the transparency of high-energy radiation. For instance, the explanation of the GRB 190114C high-energy emission needs an ultrarelativistic blastwave with a kinetic energy on the order of 10^{55} erg (see, e.g., MAGIC Collaboration 2019a,b). It is clear that such energy cannot be powered by extracting the rotational energy of a Kerr BH of a few M_{\odot} , which will be a few 10^{53} erg (see Eq. (21)).

We have shown that the inner engine can nicely explain the GeV emission by accelerating electrons in the vicinity of the Kerr BH, which radiate their kinetic energy gain via synchrotron emission. The number of particles needed by the inner engine to explain the observed high-energy emission is relatively low. Let us adopt the derived inner engine parameter for GRB 190114C: $M = 4.4 M_{\odot}$, $\alpha = 0.4$, and $B_0 = 4 \times 10^{10}$ G. For instance, from Eq. (17) we obtain that for this α a photon peak energy of 10 GeV is obtained for an electron pitch angle $\chi \approx 0.2^{\circ}$ (see also Fig. 2). Using Eq. (16), this implies an electron Lorentz factor $\gamma \approx 6.76 \times 10^4$, which corresponds to an

electron energy $\epsilon_e = \gamma m_e c^2 \approx 5.53 \times 10^{-2}$ erg = 3.45×10^{10} eV. Therefore, the number of such electrons needed to power the GeV emission of total energy $E_{\text{GeV}} = 1.8 \times 10^{53}$ erg $\approx 0.1 M_{\odot} c^2$, is $N_e = E_{\text{GeV}}/\epsilon_e = 3.25 \times 10^{54}$, which for ionized matter implies a mass of $m_p N_e \approx 2.73 \times 10^{-3} M_{\odot}$, where m_p is the proton mass.

Therefore, the inner engine uses a more efficient electro-dynamical process that produces observable high-energy emission in the vicinity of the BH. In fact the acceleration is not based on a bulk-expanding motion. Every single electron is accelerated from its initial velocity up to an asymptotic value defined by the maximum electric potential energy available for their acceleration, which depends only on the external magnetic field strength and the BH spin parameter; see Eqs. (8a) and (8b). These accelerated electrons radiate mainly at high energies in the GeV domain. The radiation of the inner engine (e.g., at keV to MeV energies) is negligible (with respect to the observed values). The observed radiation in the keV to MeV energy domains is explained by a different mechanism in a BdHN I; see (Rueda et al. 2020). The observed luminosity of GeV allows us to estimate the mass and spin of the BH.

We have determined the parameters of the inner engine of GRB 190114C using only the GeV emission data after the UPE phase. We asked the system to satisfy three physical conditions. First, that the GeV energetics is paid by the extractable energy of the BH (see Eq. (21)); second that the system is transparent to GeV photons produced by the synchrotron radiation of the accelerated electrons (see Eq. (24)); and third that the synchrotron radiation timescale explains the observed GeV emission timescale (see Eq. (26)) with the aid of Eq. (18). In order to be fulfilled, this last constraint implies that the GeV emission is emitted from electrons being accelerated with the appropriate pitch angles (see Figs. 2 and 3). These pitch angles occur within a cone of approximately 60° from the BH rotation axis (see Fig. 3), which is a key result for the interpretation of the morphology of the BdHN I (Ruffini et al. 2021).

From this procedure, we have obtained the inner engine parameters of GRB 190114C: $B_0 \approx 3.9 \times 10^{10}$ G, $\alpha \approx 0.41$, and $M = 4.45 M_{\odot}$. The corresponding irreducible mass of the BH is $M_{\text{irr}} = 4.35 M_{\odot}$. It is worth recalling that both M_{irr} and B_0 are kept constant and this should be all over the evolution. The corresponding BH parameters for GRB 130427A are dimensionless spin $\alpha = 0.47$, mass $M = 2.3 M_{\odot}$, and irreducible mass $M_{\text{irr}} = 2.2 M_{\odot}$ (Ruffini et al. 2019a). The above are the first two BH masses derived directly from the GRB observations, and in both cases they are above the theoretical values of the NS critical mass enforcing the validity of the BdHN I model: the BH are formed by smooth hypercritical accretion of the HN ejecta on the NS binary companion.

Since here we only used the GeV emission data, the BH parameters that we have obtained, namely mass and spin, have to be considered as lower limits. Thus, it is clear that even a slightly higher mass (or spin) of the BH can guarantee even larger and longer emission of the inner engine.

Our analysis paves the way to additional research; the data from the different energy bands (e.g., the higher energy bands; MAGIC Collaboration 2019a,b) might provide additional information on the energy distribution of the electrons injected by the electric field into the magnetic field, and on the pitch angle distribution for the synchrotron emission. Figure 3 shows, for the electromagnetic field configuration of the Papapetrou-Wald solution (see Fig. 1), the contours of constant pitch angle and constant electric energy density.

Before concluding, it is worth recalling some crucial aspects of the inner engine here applied to the case of GRB 190114C.

The nature of the emission results from considering the physical process leading to the electric and magnetic fields and the BH formation (see Sect. 3 and Rueda et al. 2020). This is fundamental to show that the emission process leading to the observed luminosity is not continuous, but discrete. The timescale of the emission in GRBs is too short to be probed directly by current observational facilities. Direct evidence of the value and discreteness might come instead from the observation of large BHs of $10^8 - 10^{10} M_{\odot}$ in AGN. For instance, in the case of M 87*, for fiducial parameters $M = 6 \times 10^9 M_{\odot}$, $\alpha = 0.1$, and $B_0 = 10$ G, the inner engine theory predicts a high-energy (GeV) emission with a luminosity of a few 10^{43} erg s^{-1} , with a timescale of up to tenths of seconds (see Table 2). Emission at higher energies (e.g., in the TeV band), would be characterized by a lower luminosity and a longer timescale. The timescale for UHECR emission is instead approximately half a day (see Table 2 and Rueda & Ruffini 2020).

We can therefore conclude, in the light of the results of this article and the previous articles in this series, that all BdHN I are powered by three independent sources of energy. The BdHN I is triggered by the SN explosion originating from the collapse of the CO_{core} generating a ν NS. The accretion of the SN onto the ν NS (see Sect. 9.2 and Ruffini et al. 2018c; Wang et al. 2019; Rueda et al. 2020), gives origin to the X-ray afterglow observed by *Swift*. The hypercritical accretion of the SN onto the binary companion NS gives origin to the BH as soon as the NS reaches the critical mass. This smooth accretion process is alternative to the direct gravitational collapse of a massive star. This happens in GRB 190114C at $t_{\text{tr}} = 1.99$ s. The further accretion of the SN ejecta onto the newly born BH generates the prompt gamma-ray radiation observed in GRB 190114C between 1.99 s and 3.99 s (Moradi et al., in prep.). The further accretion of the SN ejecta onto the newly born BH leads to a process of energy extraction from the inner engine that generates the jetted high-energy (\geq GeV) emission. This radiation, as is shown in this article using the Papapetrou-Wald solution (see Sect. 2), is emitted close to the BH horizon and within an angle of nearly 60° from the BH rotation axis (see Sect. 5 and Fig. 3).

Acknowledgements. We thank the Referee for the reiterated suggestions which have certainly improved the presentation of our results. An extended correspondence with the Referee has been addressed since our initial submission in order to broaden the context of our work with respect to the previous literature and which have materialized in Sect. 9.

References

- Bardeen, J. M. 1970, *ApJ*, 162, 71
- Bardeen, J. M., Press, W. H., & Teukolsky, S. A. 1972, *ApJ*, 178, 347
- Becerra, L., Cipolletta, F., Fryer, C. L., Rueda, J. A., & Ruffini, R. 2015, *ApJ*, 812, 100
- Becerra, L., Bianco, C. L., Fryer, C. L., Rueda, J. A., & Ruffini, R. 2016, *ApJ*, 833, 107
- Becerra, L., Ellinger, C. L., Fryer, C. L., Rueda, J. A., & Ruffini, R. 2019, *ApJ*, 871, 14
- Beniamini, P., Giannios, D., & Metzger, B. D. 2017, *MNRAS*, 472, 3058
- Bianco, C. L., Ruffini, R., & Xue, S.-S. 2001, *A&A*, 368, 377
- Blandford, R. D., & McKee, C. F. 1976, *Phys. Fluids*, 19, 1130
- Blandford, R. D., & Znajek, R. L. 1977, *MNRAS*, 179, 433
- Christodoulou, D. 1970, *Phys. Rev. Lett.*, 25, 1596
- Christodoulou, D., & Ruffini, R. 1971, *Phys. Rev. D*, 4, 3552
- Damour, T., & Ruffini, R. 1975, *Phys. Rev. Lett.*, 35, 463
- Daugherty, J. K., & Harding, A. K. 1983, *ApJ*, 273, 761
- de Jager, O. C., Harding, A. K., Michelson, P. F., et al. 1996, *ApJ*, 457, 253
- DeWitt, C., & DeWitt, B. S. 1973, in *Proceedings, Ecole d'Eté de Physique Théorique: Les Astres Occlus* (New York, NY: Gordon and Breach), Les Houches Summer School, 23
- Fryer, C. L., Rueda, J. A., & Ruffini, R. 2014, *ApJ*, 793, L36
- Hawking, S. W. 1971, *Phys. Rev. Lett.*, 26, 1344
- Hawking, S. W. 1972, *Commun. Math. Phys.*, 25, 152
- Kelner, S. R., Prosekin, A. Y., & Aharonian, F. A. 2015, *AJ*, 149, 33
- Kerr, R. P. 1963, *Phys. Rev. Lett.*, 11, 237
- Landau, L. D., & Lifshitz, E. M. 1975, *The Classical Theory of Fields* (Oxford: Pergamon Press)
- Liang, L., Ruffini, R., Rueda, J. A., et al. 2019, ArXiv e-prints [arXiv:1910.12615]
- MacDonald, D., & Thorne, K. S. 1982, *MNRAS*, 198, 345
- MAGIC Collaboration (Acciari, V. A., et al.) 2019a, *Nature*, 575, 455
- MAGIC Collaboration (Acciari, V. A., et al.) 2019b, *Nature*, 575, 459
- Mészáros, P., & Rees, M. J. 1997, *ApJ*, 482, L29
- Metzger, B. D., Giannios, D., Thompson, T. A., Bucciantini, N., & Quataert, E. 2011, *MNRAS*, 413, 2031
- Mirzoyan, R., Noda, K., Moretti, E., et al. 2019, *GCN Circ.*, 23701, 1
- Nakar, E. 2015, *ApJ*, 807, 172
- Nakar, E., & Piran, T. 2017, *ApJ*, 834, 28
- Newman, E. T., Couch, E., Chinnapared, K., et al. 1965, *J. Math. Phys.*, 6, 918
- Nousek, J. A., Kouveliotou, C., Grupe, D., et al. 2006, *ApJ*, 642, 389
- Papapetrou, A. 1966, *Annales de L'Institut Henri Poincaré Section (A) Physique Théorique*, 4, 83
- Ramirez-Ruiz, E., Celotti, A., & Rees, M. J. 2002, *MNRAS*, 337, 1349
- Rees, M. J., & Meszaros, P. 1992, *MNRAS*, 258, 41P
- Ruderman, M. A., & Sutherland, P. G. 1975, *ApJ*, 196, 51
- Rueda, J. A., & Ruffini, R. 2012, *ApJ*, 758, L7
- Rueda, J. A., & Ruffini, R. 2020, *Eur. Phys. J. C*, 80, 300
- Rueda, J. A., Ruffini, R., Karlica, M., Moradi, R., & Wang, Y. 2020, *ApJ*, 893, 148
- Ruffini, R., & Wheeler, J. A. 1971a, *Phys. Today*, 24, 30
- Ruffini, R., & Wheeler, J. A. 1971b, *ESRO*, 52, 45
- Ruffini, R., & Wilson, J. R. 1975, *Phys. Rev. D*, 12, 2959
- Ruffini, R., Salmonson, J. D., Wilson, J. R., & Xue, S.-S. 1999, *A&AS*, 138, 511
- Ruffini, R., Salmonson, J. D., Wilson, J. R., & Xue, S.-S. 2000, *A&A*, 359, 855
- Ruffini, R., Wang, Y., Enderli, M., et al. 2015, *ApJ*, 798, 10
- Ruffini, R., Wang, Y., Aimuratov, Y., et al. 2018a, *ApJ*, 852, 53
- Ruffini, R., Becerra, L., Bianco, C. L., et al. 2018b, *ApJ*, 869, 151
- Ruffini, R., Karlica, M., Sahakyan, N., et al. 2018c, *ApJ*, 869, 101
- Ruffini, R., Moradi, R., Rueda, J. A., et al. 2019a, *ApJ*, 886, 82
- Ruffini, R., Melon Fuksman, J. D., & Vereshchagin, G. V. 2019b, *ApJ*, 883, 191
- Ruffini, R., Moradi, R., Rueda, J. A., et al. 2021, *MNRAS*, in press [arXiv:2103.09142]
- Sari, R. 1997, *ApJ*, 489, L37
- Sari, R., & Piran, T. 1995, *ApJ*, 455, L143
- Sari, R., Piran, T., & Narayan, R. 1998, *ApJ*, 497, L17
- Sturrock, P. A. 1971, *ApJ*, 164, 529
- Tursunov, A., & Dadhich, N. 2019, *Universe*, 5, 125
- Wald, R. M. 1974, *Phys. Rev. D*, 10, 1680
- Wang, Y., Rueda, J. A., Ruffini, R., et al. 2019, *ApJ*, 874, 39
- Waxman, E., & Piran, T. 1994, *ApJ*, 433, L85
- Wijers, R. A. M. J., Rees, M. J., & Meszaros, P. 1997, *MNRAS*, 288, L51
- Woosley, S. E. 1993, *ApJ*, 405, 273
- Zhang, B. 2018, *The Physics of Gamma-ray Bursts* (Cambridge: Cambridge University Press)
- Zhang, B., Fan, Y. Z., Dyks, J., et al. 2006, *ApJ*, 642, 354